Faraday Discussions

Accepted Manuscript

This manuscript will be presented and discussed at a forthcoming Faraday Discussion meeting. All delegates can contribute to the discussion which will be included in the final volume.

Register now to attend! Full details of all upcoming meetings: http://rsc.li/fd-upcoming-meetings

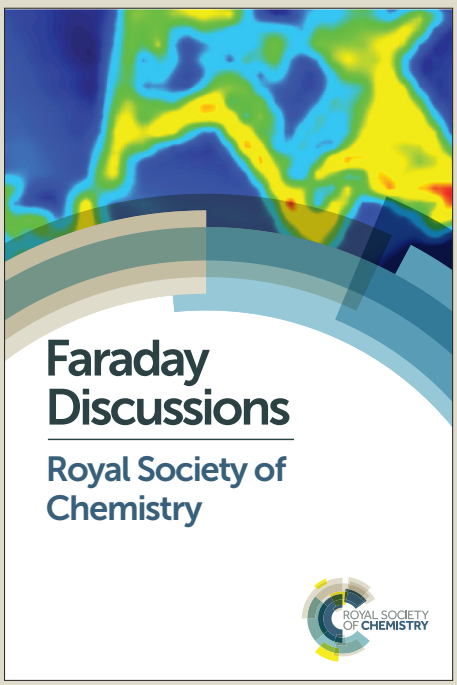

This is an *Accepted Manuscript*, which has been through the Royal Society of Chemistry peer review process and has been accepted for publication.

Accepted Manuscripts are published online shortly after acceptance, before technical editing, formatting and proof reading. Using this free service, authors can make their results available to the community, in citable form, before we publish the edited article. We will replace this *Accepted Manuscript* with the edited and formatted *Advance Article* as soon as it is available.

You can find more information about *Accepted Manuscripts* in the Information for Authors.

Please note that technical editing may introduce minor changes to the text and/or graphics, which may alter content. The journal's standard Terms & Conditions and the Ethical guidelines still apply. In no event shall the Royal Society of Chemistry be held responsible for any errors or omissions in this *Accepted Manuscript* or any consequences arising from the use of any information it contains.

ROYAL SOCIETY OF CHEMISTRY

www.rsc.org/faraday_d

HIGH RESOLUTION FTIR IMAGING PROVIDES AUTOMATED DISCRIMINATION AND DETECTION OF SINGLE MALARIA PARASITE INFECTED ERYTHROCYTES ON GLASS

David Perez-Guaita[1], Dean Andrew[2], Philip Heraud[1], James Beeson[2,3,4], David Anderson[2], Jack Richards[2,3,4] and Bayden R. Wood[1]*

[1] Centre for Biospectroscopy, Monash University, Clayton, 3800, Victoria, Australia

[2] Centre for Biomedical Research, Burnet Institute, Melbourne, 3004, Victoria, Australia

[3]Department of Microbiology, Monash University, Clayton, 3800, Victoria, Australia

[4]Department of Medicine, University of Melbourne, Parkville, 3050, Victoria, Australia

ABSTRACT

New highly sensitive tools for malaria diagnostics are urgently needed to enable the detection of infection in asymptomatic carriers and patients with low parasitemia. In pursuit of a highly sensitive diagnostic tool that can identify parasite infections at the single cell level, we have been exploring Fourier Transform Infrared (FTIR) microscopy using a Focal Plane Array (FPA) imaging detector. Here we report for the first time the application of a new optic configuration developed by Agilent that incorporates 25× condenser and objective Cassegrain optics with a high numerical aperture (NA=0.81) along with additional high magnification optics within the microscope to provide 0.66 micron pixel resolution (total IR system magnification of 61x) to diagnose malaria parasites at the single cell level on a conventional glass microscope slide. The high quality images clearly resolve the parasite's digestive vacuole demonstrating sub-cellular resolution using this approach. Moreover, we have developed an algorithm that first detects the cells in the infrared image, and secondly extracts the average spectrum. The average spectrum is then run through a model based on Partial Least Squares-Discriminant Analysis (PLS-DA), which diagnoses unequivocally the infected from normal cells. The high quality images, and the fact this measurement can be achieved without a synchrotron source on a conventional glass slide, shows promise as potential gold standard for malaria detection at the single cell level.

KEYWORDS

Malaria diagnostic, Fourier Transform infrared (FTIR) spectroscopy, FTIR imaging, Focal Plane Array, single cell

Introduction

Malaria remains one of the most devastating diseases to afflict humanity. In 2015, there were approximately 214 million reported cases of malaria resulting in 438 000 deaths.[1] Most deaths occur in children under 5 years of age with approximately 90 % of cases occurring in Sub-Saharan Africa.[1] Much progress has been made in recent years in decreasing this burden and this has led to a strong global commitment to malaria elimination. Achieving this objective will require highly sensitive diagnostics that detect low-density parasitemia in asymptomatic carriers (i.e. people who have contracted the infection but do not express the clinical symptoms of chills and fevers). These individuals currently provide a vast submicroscopic reservoir of infection that is transmissible to mosquitoes. Identifying and treating these individuals will require diagnostics that can be used for rapid mass screening at very low cost. Routine tests for malaria screening include optical microscopy,[2] Rapid Diagnostic Tests (RDTs) based on antigen capture[3] and nucleic acid amplification like Polymerase Chain Reaction (PCR).[4, 5] Optical microscopy on thick blood films is a relative inexpensive technique but requires an experienced microscopist to make the diagnosis and has a reported sensitivity of 5-10 parasites/μL.[6] RDTs are used worldwide but are often limited in their sensitivity and ability to identify multiple species of *Plasmodium*. RDTs are very cheap, ~USD $2, but take 15-25 minutes to obtain a result and provide no quantitative information on the level of parasitemia.[3] PCR amplification is the current gold standard with a detection limit of 1 parasite/μL but needs multiple primers to speciate, is costly and requires considerable technical expertise. In pursuit of a new diagnostic tool we have trialled a number of spectroscopic approaches including Raman and Fourier Transform Infrared (FTIR) spectroscopy. These techniques rely on the detection of vibrating functional groups characteristic of the parasite.

Raman spectroscopy can be applied to diagnose parasites in single erythrocytes.[7-17] The technique principally relies on the detection of the haemozoin chromophore, which forms as a by-product from the digestion of haemoglobin by the parasite. The technique can detect early blood-stage parasites, providing they have haemozoin crystal clusters in the order of 300 nm. Consequently it is not good at detecting early stage rings and gametocytes, which are the dominant forms of the parasite found in peripheral blood in

Plasmodium falciparum. Surface Enhanced Raman Spectroscopy (SERS)[18-20] and Tip Enhanced Raman Spectroscopy (TERS)[21] have the potential to detect smaller haemozoin inclusions but the expense and complexity of the measurement make it difficult to implement in a hospital. The other consideration is the time taken to analyse a field of cells with this technique, which can take several hours. Raman acoustic levitation spectroscopy (RALS) has shown potential to diagnose haemozoin from a lysed pellet of erythrocytes[13] but the levitated blood drop can become unstable and explode making it unsafe to the health worker.

In pursuit of a more routine spectroscopic approach that does not rely solely on the presence of haemozoin, we have investigated the potential of Fourier Transform Infrared (FTIR) spectroscopy.[22-24] Unlike Raman spectroscopy, which is a scattering based technique; FTIR relies on the detection of functional groups absorbing infrared photons. The technique is very suited to detecting functional groups that have a strong change in their dipole moment as the molecule vibrates. Consequently, proteins, nucleic acids, lipids and carbohydrates are all good infrared absorbers and provide distinct markers for malaria parasites, especially when the technique is used on isolated erythrocytes, which contain haemoglobin but no nucleus or other large organelles to confound the diagnosis. By applying synchrotron FTIR transmission spectroscopy with a neural network we were able to discern rings, trophozoites, and schizonts with very high specificity on a thin film of cells fixed in methanol on CaF_2 windows.[23] Using Attenuated Total Reflection (ATR-FTIR) spectroscopy we have demonstrated a detection limit of 0.00001 % parastemia (0.1 parasites per μL) and a quantification limit of 0.001 % a parastemia (10 parasites per μL) using spiked isolated erythrocytes fixed in methanol.[22] More recently we utilised an FTIR microscope equipped with a Focal Plane Array (FPA) detector coupled to a synchrotron light source at the IRENI beamline located in the former Synchrotron Radiation Centre, University of Wisconsin-Madison, to image and diagnose single cells infected with the malaria parasite. The microscope was fitted with a 74 x Cassegrain objective (Ealing Inc., Rocklin, CA, USA) with a Numerical Aperture (NA= 0.65) resulting in a pixel size of 0.54 μm. While the images showed that single cells could be resolved, it did not resolve subcellular detail and individual parasites could not be identified within single cells. The substrate used in this case was BaF_2, which is very expensive for routine measurements. More recently Bassan et al.[25] showed the potential of using glass-based substrates for FTIR imaging of tissue biopsies. The strong absorbance from the Si-O bonds in glass resulted in only the 3800-

2500 cm^{-1} spectral range being diagnostically useful, however, the authors demonstrated that tissue could be classified into four basic tissue cell types and that using just the epithelial cells, reasonable discrimination of normal and malignant breast tissue could be found.

Recently Agilent developed a new 25 × Cassegrain objective with a high NA = 0.81 for their Agilent Cary 620 microscope. The high NA of this objective coupled with a high magnifications optics within the microscope enables a pixel size of 0.66 μm, providing a total IR system magnification of 61x. Recently Reddy et al.[26] demonstrated that pixel size of 0.6 μm provides the ideal degree of spatial oversampling for a NA=0.81 system, for truly diffraction limited imaging. Pixel sizes smaller (or magnification higher) than this results in over-sampling and no improvement in image quality. over-sampling and no improvement in image quality could be achieved above this NA. In this paper, we show unprecedented image quality of single malaria infected erythrocytes recorded on a glass substrate and demonstrate how FTIR imaging can be used to diagnose infected cells from the extracted spectra using Partial Least Squares-Discriminant Analysis (PLS-DA).[27] The extremely high resolution on cheaper glass substrates paves the way forward for single cell diagnosis with an affordable substrate. Moreover, the extremely high spatial resolution enables distinct visualisation of the parasite's digestive vacuole within the fixed cell, demonstrating subcellular imaging on a blood cell for the first time.

2. Experimental

2.1 Sample preparation

Blood was collected from Melbourne control patients into lithium heparin vacutainers (BD) and centrifuged at 1500 rpm for 5 minutes to remove plasma. Blood was cultured at 3% haematocrit in RPMI media supplemented with 10% AlbuMAX II (Gibco) and infected with *Plasmodium falciparum,* laboratory strain D10. Thin blood smears of malaria parasite infected erythrocytes were air dried for 20 minutes, then fixed in 100% methanol for 5 minutes.

2.2 Infrared microscopy and image acquisition.

Infrared images were obtained using an Agilent (Santa Clara, USA) Cary 620 microscope equipped with a 25× Cassegrain objective upgraded with a high magnification optics within the microscope providing a 5x magnification boost over the "standard magnification" mode. Hyperspectral images were recorded using transmission geometry at a resolution of 4 cm^{-1} in the glass transparent region (3600-2500 cm^{-1}) by co-adding 400 interferograms. The applied zero filling factor of 2 provided 572 points per spectrum. The same configuration was used for recording a background image from a clean region on the glass slide. The 128 × 128 pixels of the FPA detector of the microscope covered a region of 102.2 × 102.2 μm of the slide and mosaics of 3 × 2 tiles were obtained. After image acquisition the slides were stained with 10% of Giemsa stain for 5 minutes, and visual images were captured for identification of the parasitized cells.

2.3 Data analysis

Hyperspectral images of the mosaics were imported to *Matlab* v2014b from *Mathworks* (Natik, USA). The data processing was carried out using in-house Matlab scripts and functions available in the *PLStoolbox* v7.0 package from *Engeinvector* (Manson, USA). For the single erythrocytes spectroscopy (results section 3.1), the function *improfile* was used for obtaining the profile of the images. Images were resized to five times the original size using the *imresize* function prior to the circle identification. The function *imfindcircles* was applied to detect circles with a radius ranging between 23 to 28 pixels (3.7- 4.5 micrometres). For the intracellular resolution (results section 3.2), noise reduction was applied using the first 20 PCs prior to the PLS-DA. The PLS-DA was performed over the 3400-2800-cm^{-1} region using a 25 point Savitzky-Golay smoothing filter, a baseline correction procedure (based on an automatic weighted least squares routine) and mean centring. For the detection of infected erythrocytes from their average spectrum (results section 3.3), PLS-DA was carried out between 3400-2800 cm^{-1}, using a 21 points Savitzky-Golay smoothing filter and standard normal variate normalization. The noise in the spectra necessitated excessive smoothing. The tuning parameters for the PLS-DA (e.g. number of latent variables regions and pre-processing methods)

were selected according to visual inspection of the spectra and the cross-validation error, with smaller cross-validation errors for the more robust models.

3. Results

3.1 Single erythrocyte spectroscopy

The high magnification imaging configuration was able to provide sufficient spatial resolution to ensure that a group of spectra corresponded to a single cell. By applying chemometric analysis a snapshot of the metabolic composition of each cell could be obtained. Single cell resolution using conventional IR microscopy with standard 15 x Cassegrain optics is problematic due to the small size of the erythrocytes (~7 μm in diameter), which is at the limit of the spatial resolution of IR light.[28] In order to investigate the absolute spatial resolution that could be achieved using this optic configuration we performed oversampling of the image. Figure 1 depicts different maps extracted from the hyperspectral image of three cells. The visible image (Figure 1a) highlights cells adjacent to each other and exemplifies the capability of the methodology for distinguishing between contiguous erythrocytes. The following figures show the false-colour map representing the integrated area between 3600-2500 cm^{-1} of the absorbance spectra (Figure 1b); along with the integrated area of the Amide A band, which is assigned principally to the N-H stretching modes of proteins (Figure 1c); and the C-H stretching region from lipids (Figure 1d). A visual inspection of the maps indicates that each erythrocyte comprised of 75-100 pixels, depending on the diameter of the cell, and was clearly distinguishable from adjacent cells, with a gap of 1.4 μm (i.e. two pixels). The visual discrimination is wavelength dependent and is therefore poorer in the C-H region (3100-2800 cm^{-1}) compared to the Amide A region (3600-3200 cm^{-1}). The poor signal-to-noise ratio of the C-H bands further reduces the contrast of the image because the absorbance values are in general three times lower than the absorbance values of the Amide A band.

Figure 1e shows the normalised profiles generated by taking a line of spectra through the three cells (indicated on the figures as a dashed line). The three cells are clearly resolved with the nodes at approximately 10 and 20 μm, corresponding to the adjacent edges of the cells.

The capability of software routines to extract the spectra of individual cells was assessed so that images could be automatically processed mitigating the need for human analysis. The ability for the *imfindcircles* function from *Matlab* for identifying and selecting pixels for each cell was assessed (Figure 2). Although the cells were well defined, when using the integrated area between 3600-2500 cm^{-1}, the software was only able to detect 26 of the 32 erythrocytes observed in the visible image. In addition, some cells were detected twice. This is likely due to the spectra containing contributions from light dispersion in the phase component of the spectrum in addition to the absorbance part of the spectrum. The extent of the light dispersion strongly depends on the shape and thickness of the cells. The cell detection algorithm was very sensitive to the shape of the cells, with the diagnostic potential of the technique compromised when cells were not spherical. The infrared images obtained from the integration of the C-H stretching region did not provide enough discrimination for the identification of the individual cells due to the wavelength dependence of the resolution and the low absorbance in this region. However, in the case of the Amide A images, all the cells were detected using the algorithm, demonstrating the images had the required spatial resolution for automatic detection of individual cells.

3.2 Intracellular resolution

Mature trophozoites were investigated to determine if subcellular structures like the digestive vacuole could be identified. An example of a cell infected with a trophozoite is shown in Figure 3a. Plots of the integrated area (3600-2500 cm^{-1}, z-spatial direction) versus spatial position (x,y) of the trophozoite shows the digestive vacuole as a "hole", which correlates to a reduction in optical density. Images of six infected erythrocytes were used to generate a false-colour map based on the integrated area between 3600-2500 cm^{-1} of the raw absorbance spectrum for each pixel (Figure 3b). These data therefore contains both absorption and scattering effects. Warm colours indicate a high quantity of organic matter, while cold colours represent an absence of it. It can be seen that the parasite shows a significant decrease in organic matter in the region of the vacuole, which can be detected as a circular-shaped hole in each of the infrared images.

Figure 4 shows maps of 9 infected erythrocytes generated by integrating the area between 3600-2500 cm^{-1}. The digestive vacuole of each trophozoite is clearly resolved in the images and circled in red, while the erythrocyte cytoplasm is circled in blue. The spectral information extracted from these circled areas was

poor and no significant chemical differences were observed between the parasite and the cytoplasm of the cell. Maps based on the integration of bands and other unsupervised multivariate procedures were also assessed for finding chemical differences between the regions but were also unsuccessful, in part due to the low signal-to-noise ratio of the pixels in the digestive vacuole region. To enhance the probability of detecting chemical differences between infected and uninfected cells a supervised multivariate modelling approach was employed.

Partial least squares-discriminant analysis (PLS-DA) is a supervised approach where the loadings are weighted to enhance the discrimination. PLS-DA was performed using 9 infected erythrocytes. The important spectral features assigned to normal erythrocytes cytoplasm (mainly haemoglobin) and the trophozoite's digestive vacuole are shown in Figure 5. Seventy-three pixels were assigned to the trophozoite vacuole and 200 pixels to the regular erythrocytes cytoplasm. A cross validation PLS-DA model was built using 5 latent variables and showed 81% specificity and 83% sensitivity. In this study, sensitivity and specificity were defined as the true positive and true negative rate obtained by comparing the values predicted by the model to the actual values obtained using a visual inspection of the stained cells. A permutation test, developed by our group,[29] found the model to be significant ($p<0.005$). Figure 5 shows the regression vector for the classification along with the mean spectrum of the samples. The bands responsible for the classification are: a) the C-H bands at 2914 cm^{-1}, 3150 cm^{-1} and 3028 cm^{-1} ; b) a shift in the Amide A band centred at 3300 cm^{-1}. Strong loadings are located at 2914 cm^{-1} and 3150 cm^{-1} and the weaker loading at 3028 cm^{-1} are attributed to a higher concentration of unsaturated fatty acids in the region infected by the parasite, as evinced by the broad band at 2914 cm^{-1} (assigned to CH_2 stretching vibration) along with bands at 3150 cm^{-1} and 3028 cm^{-1} (assigned to C=C-H stretching vibration), which are typically found in triglycerides and unsaturated fatty acids. The redshift of the Amide A band in the region of the parasite compared to the corresponding band in the uninfected part of the cell is possibly due to changes in the conformation of the proteins in the presence of the parasite.

3.3 Detection of infected erythrocytes from their average spectrum

The spectra from the photomicrographs of 14 infected and 34 uninfected cells were manually selected (Supporting Information Figure S1). The mean spectra of uninfected cells (denoted by black numbers) were

extracted from the area contained by the blue circles and the mean spectra of the infected cells (denoted as blue numbers) were extracted from the area contained by the pink circles. The average spectra extracted from the infected cells had a better signal-to-noise ratio (average of 60 to 80 spectra) and were considered to be representative of the entire cells macromolecular chemistry.

The leave-one-out PLS-DA cross validation model showed an 87% classification rate (88% specificity and 87% sensitivity) and the permutation test performed (n=200) indicated that this value was statistically significant ($p<0.005$). The receiver operating curve (ROC) for the cross validation is shown (Figure 7). This curve represents the different true positives and true negatives rates obtained when a threshold (in our case the y-cross validation limit value) is varied. These results demonstrate the capability of the imaging methodology for differentiating between infected and non-infected cells. The regression vector depicts the bands responsible for the separation (Figure 8). The bands at 3300, 2952 and 2870 cm^{-1} are characteristic of uninfected cells. These bands can be assigned to the Amide A and the CH_3 symmetric and asymmetric stretching vibrations, respectively. Other bands correlated with the presence of the parasite include those at 2922 cm^{-1} and 2850 cm^{-1}, which are assigned to the symmetric and antisymmetric stretching modes of the CH_2 group. As stated above, the CH_3 and amide bands are from proteins while the presence of CH_2 suggests the formation of long chain fatty acids and triglycerides. These results indicate a change in the lipid to protein ratio, caused for the consumption of haemoglobin by the parasite.

It is to be noted that there are differences between the regression vector for the first model where the classification was performed on the visible parasite subcellular structure against rest of cytoplasm of the red blood cell, and the second classification model performed on the average spectrum of the infected erythrocytes against average spectrum of uninfected erythrocytes. In regards to the position of the Amide A, in the first classification model there was a redshift in the case of the parasite pixels, while in the second classification there was a general increase in absorption of the Amide A mode in the uninfected cells. In addition, the band assigned to the C=C-H stretching mode noted in the first model disappears for the classification performed between cells in the second model. This may be explained by the fact that the differences are more subtle when comparing different regions within the cell. In contrast, when comparing the average spectrum from whole cells the differences are dominated by the major metabolic and phenotypic

changes of the entire parasite-host system rather than changes in the haemoglobin to lipid ratio within a single cell.

4. Conclusions

We have demonstrated that high-resolution infrared images of single cells on a glass slide can be obtained using an FPA with a conventional globar IR source by incorporating a 25 × high numerical aperture (NA=0.81) Cassegrain objective system. The use of an inexpensive glass slide, as opposed to expensive IR transmission slides, offers a number of advantages in terms of cost and following current clinical practises for thick and thin film blood smears. The use of an inexpensive glass slide, as opposed to expensive transmission windows, offers a number of advantages in terms of cost and following current clinical practises for thick and thin film blood smears. The high quality images could resolve the digestive vacuole of the trophozoite demonstrating sub-cellular resolution. Moreover, the high-resolution images of the individual cells enabled the successful application of an algorithm to auto-detect individual cells from absorbance maps based on wavenumber values greater than 3500 cm^{-1}. The spectra could then be extracted from all of the pixels associated with that cell, averaged and modelled using PLS-DA, which achieved an 87 % classification rate for a leave-out-one cross-validation. The main differences identified related to: i) changes in the Amide A band, possibly due to protein conformational changes caused by the parasite and ii) more unsaturated fatty acids in the infected cells. More work is required to ascertain if the approach can be used to identify early ring stage parasites and the more elongated gametocyte forms found in peripheral blood but these initial studies demonstrate the potential of high resolution FPA imaging for single cell diagnosis on a blood film.

Acknowledgments

Funding to the authors was provided by the Australian Research Council (Future Fellowship FT120100926 to BRW), National Health and Medical Research Council of Australia (Program grant and Senior Research Fellowship to JGB; Early Career Fellowships JSR; Infrastructure for Research Institutes Support Scheme Grant to the Burnet Institute); Victorian State Government Operational Infrastructure Support Grant to the Burnet Institute. We acknowledge Mr Finlay Shanks for instrumental support and Dr Mustafa Kansiz (Agilent Technologies) for loaning us the 25 x Cassegrain objectives used for the measurements.

Figure 1. High resolution infrared images of three adjacent erythrocytes. a) Visible image, b) Integrated area between 3600-2500 cm^{-1}, c) 3400-3200 cm^{-1}, d) 2990-2850 cm^{-1}, e) Profile of the false-colour images along the three cells indicated by the dashed line on figures 1b (red), 1c (green) and 1d(black).

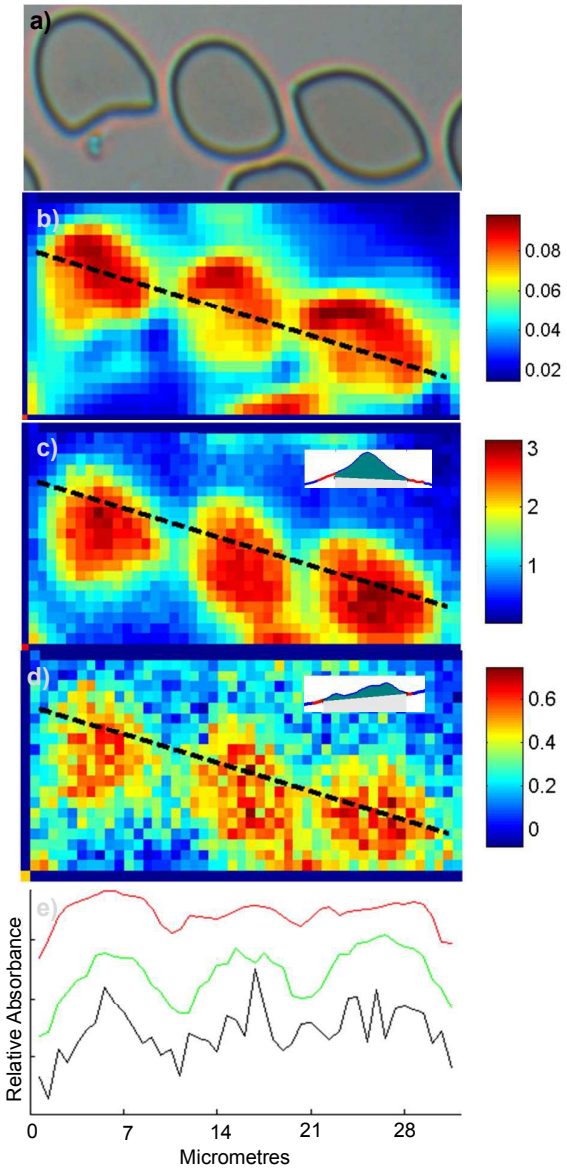

Figure 2. The automatic identification of erythrocytes in hyperspectral infrared images. a) Visible image showing a group of infected and non-infected cells. b) Integrated area between 3600-2500 cm^{-1}. c) 2990-2850 cm^{-1} d) 3400-3200 cm^{-1}. The cells identified by the *imfindcircles* function for the integrated area between 3600-2500 cm^{-1}, C-H and Amide A maps are circled in b), c) and d), respectively.

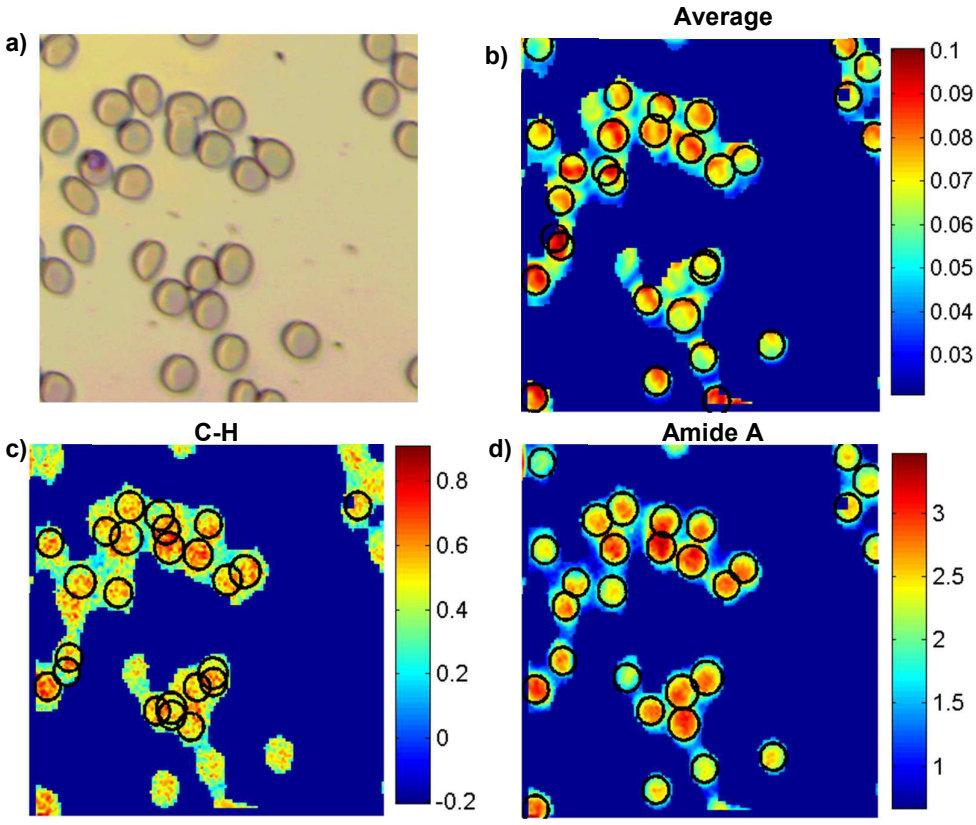

Figure 3: Infrared images of trophozoites inside infected erythrocytes. a) 3D represenation of an infected and an uninfected cell. b) False-colour images of 6 erythrocytes infected with trophozoites and their visible images. Colour scale corresponding to the integration area underneath each spectrum (pixel).

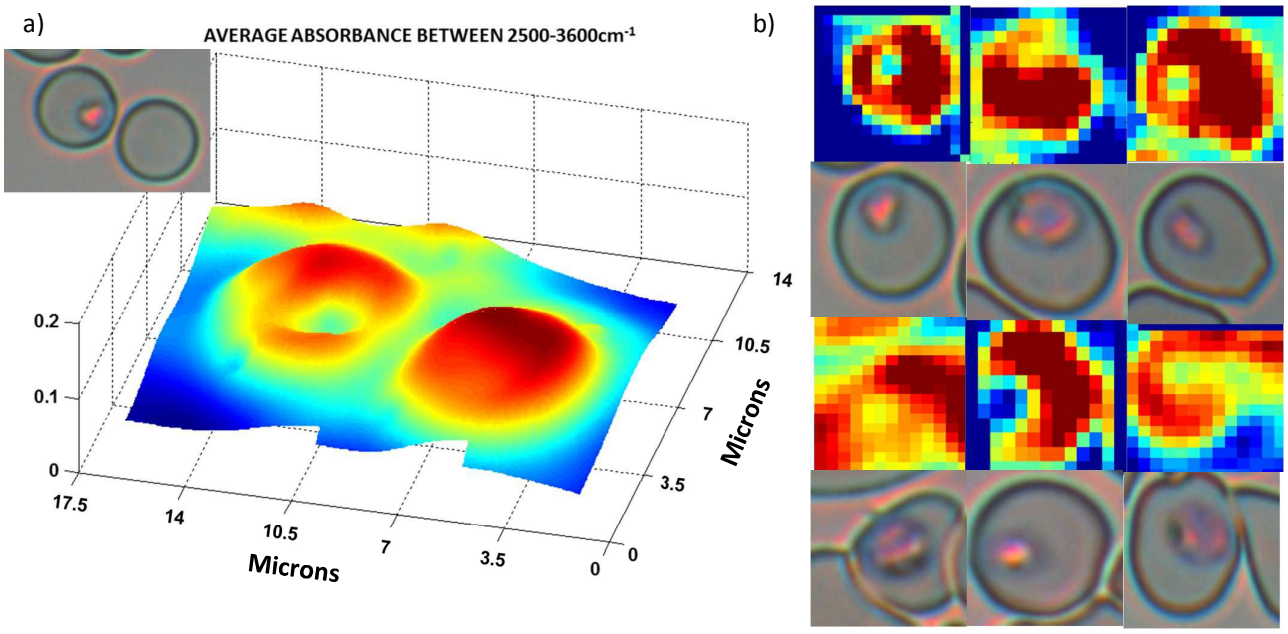

Figure 4. Regions selected as trophozoites (red) and erythrocyte cytoplasm (blue) for the PLS-DA performed in section 3.2.

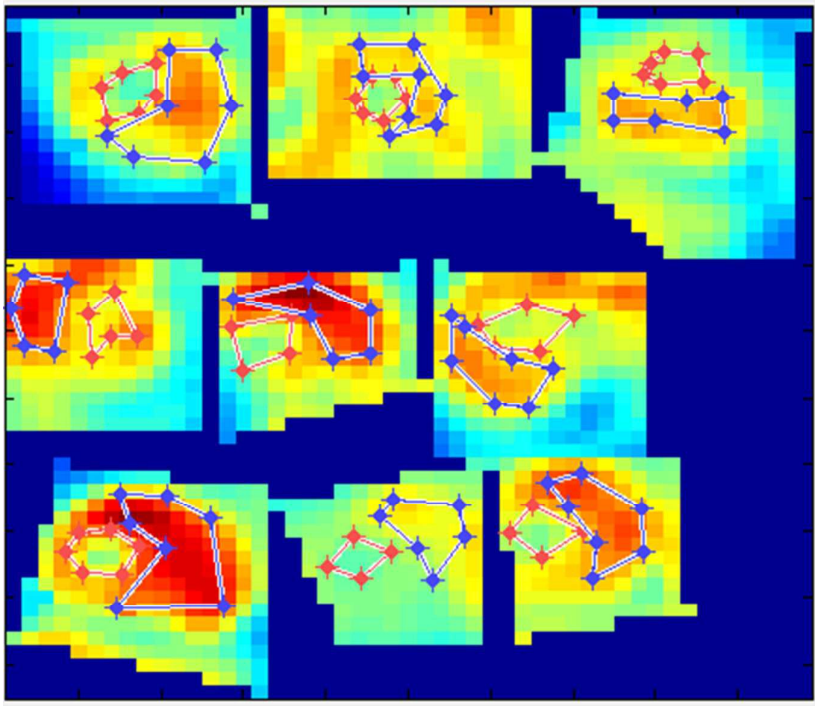

Figure 5: Regression vector for the PLS-DA model described in section 3.3. The red spectrum denotes the mean spectrum of the dataset.

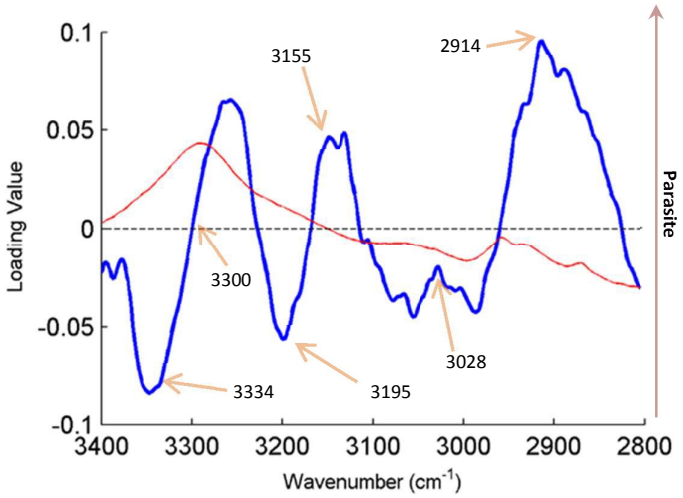

Figure 6. Receiver operating curve of the cross validation of the PLS-DA model performed on the section 3.3

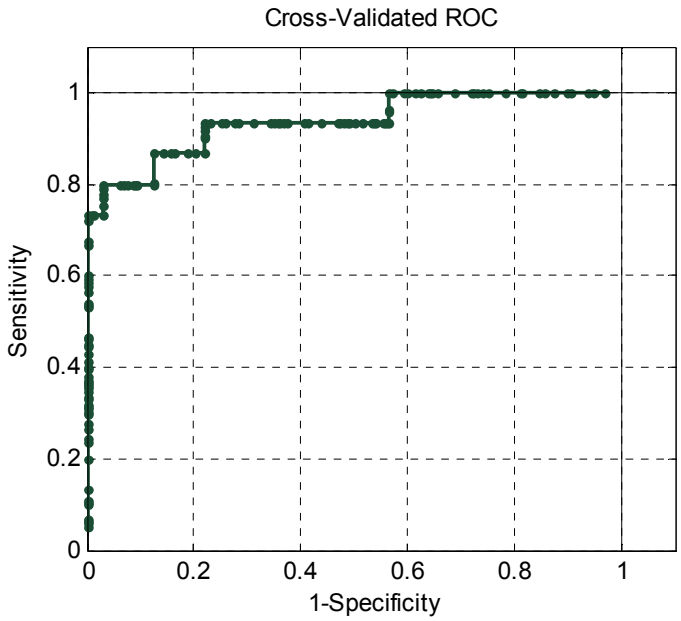

Figure 7. Regression Vector for PLS-DA model described in section 3.3. The red spectrum denotes the mean spectrum of the dataset.

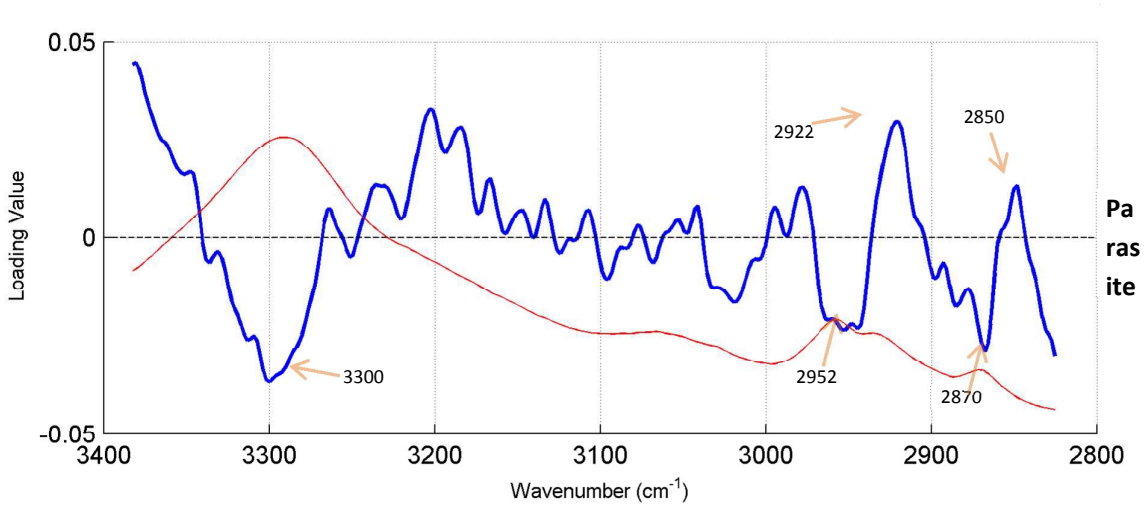

References

1. WHO, 10 facts on malaria, http://www.who.int/features/factfiles/malaria/en/).
2. B. E. Barber, T. William, M. J. Grigg, T. W. Yeo and N. M. Anstey, *Malaria journal*, 2013, **12**, 8.
3. B. E. Barber, T. William, M. J. Grigg, K. Piera, T. W. Yeo and N. M. Anstey, *Journal of clinical microbiology*, 2013, **51**, 1118-1123.
4. H. A. Dawoud, H. M. Ageely and A. A. Heiba, *Journal of the Egyptian Society of Parasitology*, 2008, **38**, 339-350.
5. H. A. Dawoud, H. M. Ageely and A. A. Heiba, *Journal of the Egyptian Society of Parasitology*, 2008, **38**, 329-338.
6. N. Tangpukdee, C. Duangdee, P. Wilairatana and S. Krudsood, *The Korean journal of parasitology*, 2009, **47**, 93-102.
7. B. R. Wood, A. Hermelink, P. Lasch, K. R. Bambery, G. T. Webster, M. A. Khiavi, B. M. Cooke, S. Deed, D. Naumann and D. McNaughton, *The Analyst*, 2009, **134**, 1119-1125.
8. B. R. Wood and D. McNaughton, *Expert review of proteomics*, 2006, **3**, 525-544.
9. M. Bilal, M. Saleem, S. T. Amanat, H. A. Shakoor, R. Rashid, A. Mahmood and M. Ahmed, *J Biomed Opt*, 2015, **20**.
10. M. Bruckner, K. Becker, J. Popp and T. Frosch, *Anal Chim Acta*, 2015, **894**, 76-84.
11. C. W. Ong, Z. X. Shen, K. K. H. Ang, U. A. K. Kara and S. H. Tang, *Appl Spectrosc*, 1999, **53**, 1097-1101.
12. C. W. Ong, Z. X. Shen, K. K. H. Ang, U. A. K. Kara and S. H. Tang, *Appl Spectrosc*, 2002, **56**, 1126-1131.
13. L. Puskar, R. Tuckermann, T. Frosch, J. Popp, V. Ly, D. McNaughton and B. R. Wood, *Lab Chip*, 2007, **7**, 1125-1131.
14. A. Schulte, F. Andrade, C. Schwarz, L. Ayong and D. Chakrabarti, *Biophys J*, 2007, 383A-383A.
15. B. R. Wood, S. J. Langford, B. M. Cooke, F. K. Glenister, J. Lim and D. McNaughton, *Febs Lett*, 2003, **554**, 247-252.
16. K. M. Marzec, D. Perez-Guaita, M. de Veij, D. McNaughton, M. Baranska, M. W. Dixon, L. Tilley and B. R. Wood, *Chemphyschem*, 2014, **15**, 3963-3968.
17. M. Kozicki, J. Czepiel, G. Biesiada, P. Nowak, A. Garlicki and A. Weselucha-Birczynska, *The Analyst*, 2015, **140**, 8007-8016.
18. N. L. Garrett, R. Sekine, M. W. Dixon, L. Tilley, K. R. Bambery and B. R. Wood, *Physical chemistry chemical physics : PCCP*, 2015, **17**, 21164-21168.
19. C. Yuen and Q. Liu, *J Biomed Opt*, 2012, **17**, 017005.
20. C. Yuen and Q. Liu, *The Analyst*, 2013, **138**, 6494-6500.
21. B. R. Wood, E. Bailo, M. A. Khiavi, L. Tilley, S. Deed, T. Deckert-Gaudig, D. McNaughton and V. Deckert, *Nano letters*, 2011, **11**, 1868-1873.
22. A. Khoshmanesh, M. W. A. Dixon, S. Kenny, L. Tilley, D. McNaughton and B. R. Wood, *Anal Chem*, 2014, **86**, 4379-4386.
23. G. T. Webster, K. A. De Villiers, T. J. Egan, S. Deed, L. Tilley, M. J. Tobin, K. R. Bambery, D. McNaughton and B. R. Wood, *Anal Chem*, 2009, **81**, 2516-2524.
24. B. R. Wood, K. R. Bambery, M. W. A. Dixon, L. Tilley, M. J. Nasse, E. Mattson and C. J. Hirschmugl, *The Analyst*, 2014, **139**, 4769-4774.
25. P. Bassan, J. Mellor, J. Shapiro, K. J. Williams, M. P. Lisanti and P. Gardner, *Anal Chem*, 2014, **86**, 1648-1653.
26. R. K. Reddy, M. J. Walsh, M. V. Schulmerich, P. S. Carney and R. Bhargava, *Appl Spectrosc*, 2013, **67**, 93-105.
27. D. Ballabio and V. Consonnia, *Anal. Methods*, 2013, **5**, 3790-3798.
28. P. Lasch and D. Naumann, *Biochimica et biophysica acta*, 2006, **1758**, 814-829.
29. D. Perez-Guaita, J. Kuligowski, S. Garrigues, G. Quintas and B. R. Wood, *The Analyst*, 2015, **140**, 2422-2427.